Investigation of Creep Damage and Cavitation Mechanisms in P92 Steels

Y. Gu, G. D. West, R. C. Thomson
Department of Materials, Loughborough University, Loughborough, LE11 3TU, UK

J. Parker
Electric Power Research Institute, 1300 Harris Boulevard, Charlotte, North Carolina, 28262, USA

ABSTRACT

In typically processed creep stress enhanced ferritic steels (CSEF) it has been observed that the long term performance and creep rupture strength is below that predicted from a simple extrapolation of the short term creep data. One of the primary microstructural degradation mechanisms responsible for this behaviour is the development of creep voids. Nucleation, growth and interlinkage of voids will also result in a significant loss of creep ductility.

In this study, the cavities in creep tested P92 steel have been characterised. It has been found that in the standard P92 samples studied, the cavities are associated with large (typically 1-2 μm) ceramic particles. Three particle compositions were observed and more detailed TEM investigations showed that these particles were BN, MnS and γ-Al_2O_3. Statistical analysis of the ceramic particle types showed that in all samples studied a very high proportion of the cavities was associated with BN particles. The shape of both the cavity and associated particle were studied in 3D using a Focussed Ion Beam/ Field Emission Gun Scanning Electron Microscope (FIB-FEGSEM) 'slice and view' technique. This showed that both the cavity and associated particle had very irregular shapes.

Analysis in the head-gauge transition area of a creep test bar, where the exposure stress is low, showed small cavities associated with the BN particles. This provides strong evidence that the cavities were preferentially nucleating on the hard, irregularly shaped BN particles.

INTRODUCTION

Creep strength enhanced ferritic (CSEF) steels are used in steam pipes, headers and tubes because of their combination of properties which include; high thermal conductivity, low thermal expansion coefficient, low susceptibility to thermal fatigue, good corrosion and oxidation resistance, and relatively good creep resistance [1, 2]. These properties derive from the microstructure, which when properly processed contains a tempered martensitic matrix containing a substructure with a high dislocation density and a fine dispersion of second phase precipitates.

However, the microstructures of CSEF steels evolve during service where the materials undergo long term creep. A number of microstructural degradation mechanisms have been identified which are thought to be responsible for the loss of long term creep strength. These include; the precipitation of new phases (e.g. Laves and Z phases), the dissolution of fine M_2X and MX

carbonitrides, the recovery of the dislocation sub-structure and the development of creep voids in the microstructure [3-6].

It has been found that the creep cavities in high Cr steels start to nucleate in the early stages of a creep test [7]. The mechanism of creep cavity nucleation in these steels is not fully established; although several possibilities have been suggested by Kassner and Hayes [8]. In P92 steels, coarse Laves phase particles have been reported to be the preferential site for cavity nucleation [9]. In this work by Lee *et al*. it was suggested that the coarsening of Laves phase to a certain size (over an average diameter of 130 nm) triggers cavity nucleation at grain boundaries resulting in brittle fracture. Zhao *et al*. [10] have suggested that inclusions, such as manganese sulphide and alumina, are the preferential nucleation sites of the creep cavities.

The addition of boron can improve the creep strength of 9% Cr steels at 650^{o}C [11]. The fine distribution of $M_{23}C_6$ carbides in the vicinity of prior austenite grain boundaries can be stabilised by boron additions during creep [12]. The benefits of boron addition are however only realised if the precipitation of BN can be avoided as this consumes soluble boron and nitrogen. The solubility of B and N is very sensitive to the absolute concentrations in the steel, and also to the temperatures used in the initial high temperature processing of the steel. It has been reported that the concentration of boron and nitrogen at which BN forms is governed by the equation log[%B]=-2.45log[%N]-6.81 [13]. Li *et al.* have calculated the boron nitride solubility at elevated temperatures (1175^{o}C to 1200^{o}C) using thermodynamic simulations which are able to take into account the full chemical composition of the steel, and particularly the W concentration which can influence the formation of tungsten borides. These calculations have resulted in a modified boron nitride solubility line [14].

The aim of the present research is to quantitatively characterise the microstructures of creep tested P92 samples to understand where the creep cavities are nucleating.

EXPERIMENTAL PROCEDURES

Table 1 gives the chemical compositions of the two P92 steels studied. The creep samples with composition A and B were normalised at 1071^{o}C and 1066^{o}C respectively and followed by a temper at 777^{o}C. Table 2 shows the creep testing conditions, reduction in area at failure, and lifetime of each sample. The samples were all observed to fail in the gauge length, which, before the creep test, had a diameter of 6 mm. These samples were selected for this study as they possessed different reductions in area in tests with durations around 10,000 hours yet had only slight variation in chemical composition.

Table 1: Chemical compositions of the P92 steels studied (wt.%), balance Fe.

	C	Mn	P	S	Si	Cr	Ni	Mo	V	Al	W	B	Nb	N
A	0.09	0.47	0.014	0.006	0.35	8.7	0.38	0.39	0.18	0.005	1.84	0.0036	0.057	0.0464
B	0.11	0.44	0.015	0.002	0.34	8.8	0.13	0.41	0.20	0.006	1.95	0.0036	0.058	0.0403

Table 2: Creep testing conditions, creep life and reduction in area at failure of the samples studied.

Sample	Composition	Temperature (^{o}C)	Stress (MPa)	Lifetime (h)	Reduction in area (%)
550-B	B	550	202	10,823	69.3
600-A	A	600	132.4	11,057	2.5
650-A	A	650	62.5	25,187	2.4

The three creep samples were cross-sectioned along the load direction using a Struers Accutom-5 cutting machine. The sectioned samples were mounted in conductive Bakelite and ground using 240 to 1200 grit SiC in resin bonded pads, followed by polishing using standard cloths with diamond suspensions down to 1 μm. An extended final polishing stage using 0.02 μm colloidal silica suspension was undertaken to provide a deformation-free surface polish.

Scanning electron microscopy was carried out in a Zeiss 1530VP field emission gun system (FEGSEM). SEM images were collected using an Everhart Thornley (ET) secondary electron (SE) detector and Solid State Backscatter detector using an accelerating voltage of 10 kV, an aperture of 60 μm and a working distance of ~12 mm. In-lens SE imaging was undertaken at short working distances also at 10 kV. The chemistry of features of interest was studied with Energy Dispersive Spectroscopy (EDS) using an Oxford Instruments X-max 80 Silicon Drift Detector (SDD), which was attached to the FEG-SEM.

An FEI Nova 600 Nanolab dual beam consisting of a Field emission Gun Scanning Electron Microscope and Focused Ion Beam System (FEG-SEM/FIB) was used for serial sectioning and preparing site specific thin foil TEM samples. For serial sectioning, a 1 μm thick layer of Pt was deposited on the area to be analysed (20 × 20 μm^2) and FIB trenches were cut with ion beam in front and to the side of the Pt layer. Serial sectioning was carried out using a current of 1 nA and SEM images were collected after each 55 nm slice. The data stack collected was reconstructed using Avizo v6 software. TEM samples were prepared using the dual beam using a standard in-situ lift out procedure.

Transmission electron microscopy (TEM) was carried out using a JEOL 2000FX microscope operating at 200 kV and equipped with an Oxford Instruments Inca EDS system. An Erlangshen ES500W digital camera was used to capture images and selected area diffraction (SAD) patterns.

Thermodynamic simulations were performed using the software package ThermoCalc in conjunction with the thermodynamic database for ferrous materials, TCFE version 6, to give an indication of the phases likely to be present at the equilibrium in the steels with the given compositions. The simulations were carried out over the temperature range 300 to 1300^{o}C.

RESULTS AND DISCUSSION

SEM Examination of Creep Cavities

Creep cavities were observed in the gauge section of all samples studied, a typical example of which is shown in Fig. 1a. A more detailed examination of this cavity using the in-lens detector in the SEM (Fig. 1b) clearly revealed that a large particle was accomodated within the cavity.

Extending this analysis to a large number of cavities revealed that large particles (~1-2 μm in diameter) were often associated with cavities, typical examples of which are shown in Fig. 2.

EDS analysis in the SEM was undertaken to determine the chemical composition of the particles within the cavities. Three discrete compositions were found which were consistent with BN, MnS and Al_2O_3 type particles. These different types of particles can also be distinguished from their appearance in the in-lens images as shown in Fig. 3.

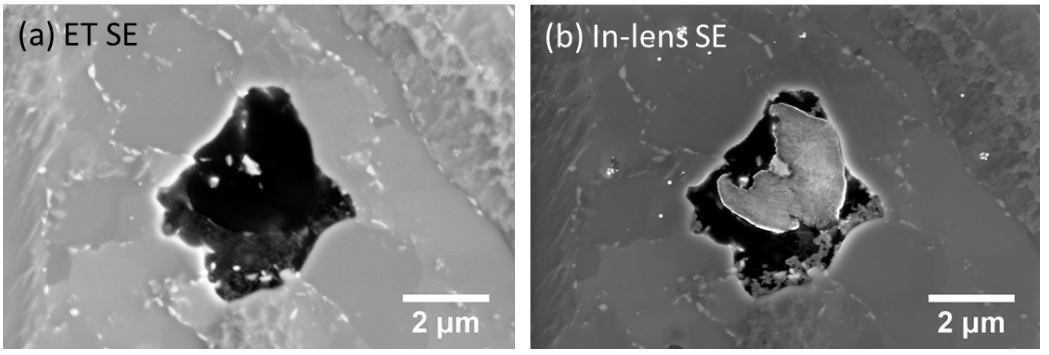

Figure 1: SEM micrographs of a cavity in sample 550-B gauge section 6 mm away from the fracture surface collected using the standard Everhart Thornley SE detector (a) and the in-lens SE detector (b).

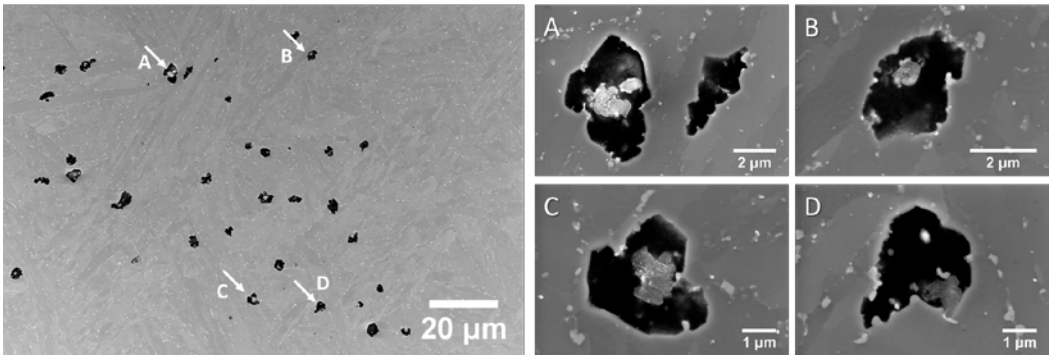

Figure 2: In-lens SEM images showing creep cavities associated with particles in the gauge section of sample 600-A. High magnification images of selected cavities are also shown.

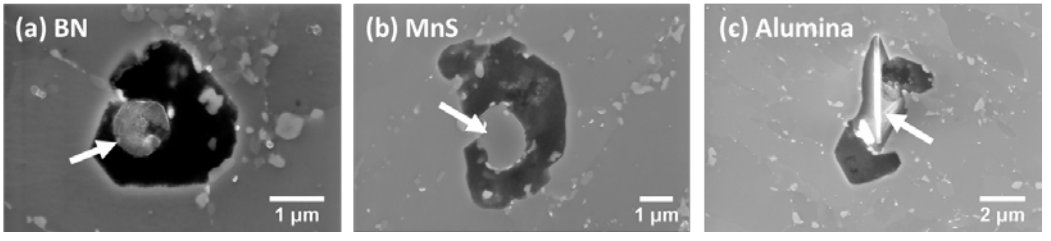

Figure 3: In-lens SEM micrographs showing the different particle types that associate with creep cavities; boron nitride (a), manganese sulphide (b), and alumina (c).

Using a combination of in-lens SEM examination and EDS, the number and type of particles that are present within the cavities was measured as a function of distance from the fracture surface. These data are shown in Table 3 and clearly show that BN-types particles are most commonly accomodated within the cavities at all distances from the fracture section. A number of cavities were also observed that did not appear to have a large particle associated with them. This is not surprising because only a 2D section across a random plane in the cavity is being examined and consquently the part of the cavity where the particle is present may not always be in this plane. This effect would be expected to become more significant with increasing cavity size and this is indeed what was observed. For example, the effect is more significant in the low ductility samples 600-A and 650-A, whose cavities are larger in size and more in number than the high ductility sample 550-B.

Table 3: The number density of cavities and associated particle types as a function of distance from the fracture surface in the three samples.

Sample	Distance to fracture surface	Number of cavities per ~50000 μm^2	BN	MnS	Al_2O_3	Not detected
550-B	1 mm	60	25	6	2	27
	3 mm	47	34	1	2	10
	5 mm	51	41	1	1	8
	7 mm	42	26	3	2	11
	9 mm	36	30	1	1	4
600-A	1 mm	159	43	10	3	103
	3 mm	108	32	7	3	66
	5 mm	119	41	11	2	65
	7 mm	79	35	6	1	37
	9 mm	100	18	9	4	69
650-A	1 mm	90	27	10	2	51
	3 mm	76	30	8	4	34
	5 mm	74	17	9	4	44
	7 mm	90	31	7	6	46
	9 mm	83	35	9	2	37

3D Examination of Cavities

In order to study the association of cavities with particles more completely, 3D analysis was undertaken using a FIB based serial sectioning technique. This technique involved slicing using the FIB and imaging using the SEM until a large particle was present in the cavity. The composition of the particle was then measured using EDS, and then the FIB sectioning and SEM imaging processes were completed so that a full set of slices of the particle were collected so that the shape of the cavity and associated particle could be determined. In the example shown in Fig. 4 for sample 600-A, 6 mm from the fracture face, the particle was identified as BN. Out of 26 particles analysed in this way 18 were BN, 1 was alumina and 3 were MnS. On some occasions more than one particle type was observed, in which case the cavity was classified as being associated with the largest particle present. In four cavities no ceramic particles were detected, although it is possible that they were present because detecting small low atomic weight elements such as B and N in serial section experiments is not straightforward. It can however be clearly concluded that the proportion of cavities with BN particles present is much higher than was observed in the 2D planar surface analysis.

From the 3D data collected, the shape of the creep cavities and the associated particles was reconstructed. An example of such a reconstruction is shown in Fig. 5. In the reconstruction shown, the cavity has a diameter of around 2 µm, whereas that of the BN particle is around 1-1.5 µm. Much smaller second phase particles including Laves phase were found to decorate the inner wall of the cavities.

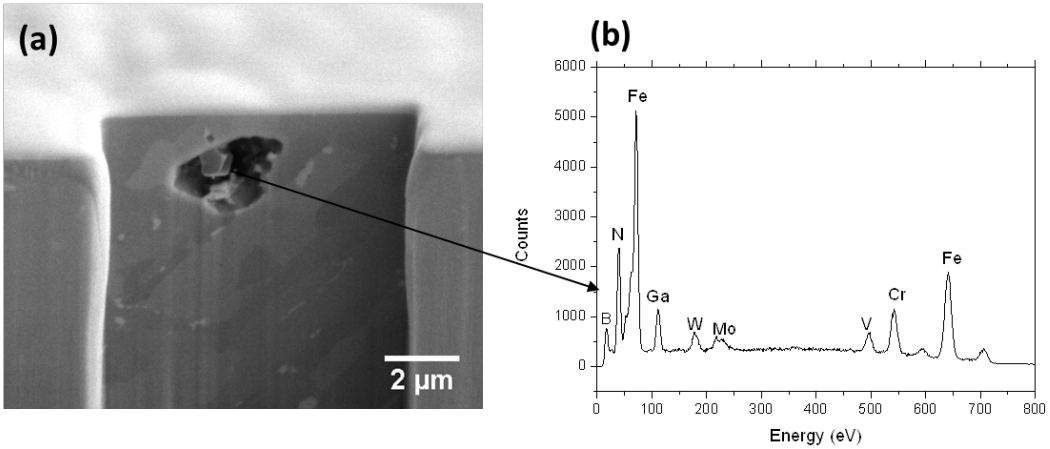

Figure 4: An SEM micrograph of a FIB prepared cross-section of a cavity and associated BN particle in 600-A 6 mm away from the fracture section (a). The EDS spectrum with clear B and N peaks is shown in (b).

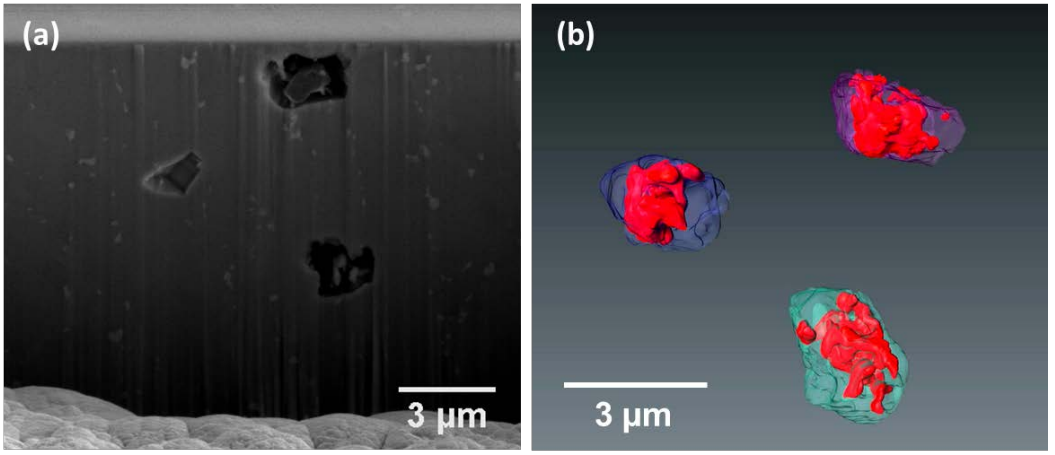

Figure 5: An example of a single SEM cross-section slice taken in sample 600-A 6 mm away from fracture surface (a). A reconstruction of the data stack showing the pore (shown in blue, purple and green) and associated particle (shown in red) in 3D.

TEM Analysis of the Particles Associated with Cavities

Although the approximate composition of the particles associated with the cavities could be determined using EDS in the SEM, the composition and crystallography of the phases was determined more comprehensively using TEM. Site specific TEM samples were prepared in cavities containing each of the three particles types associated with them. Bright field TEM micrographs, selected area diffraction patterns and EDS spectra for each particle type are shown in Fig. 6. The BN particles were shown to contain just B and N and had a hexagonal crystal structure. The MnS phase was shown to have a face-centred-cubic (FCC) structure and have a small amount of Ca contained within the phase. The alumina phase had an FCC structure consistent with γ-alumina (lattice parameter of 7.9 Å) and small amount of Mg and Ca were observed in this phase. γ-Al_2O_3 inclusions have previously been reported in steels and form from the retained slag in the steel making process [15].

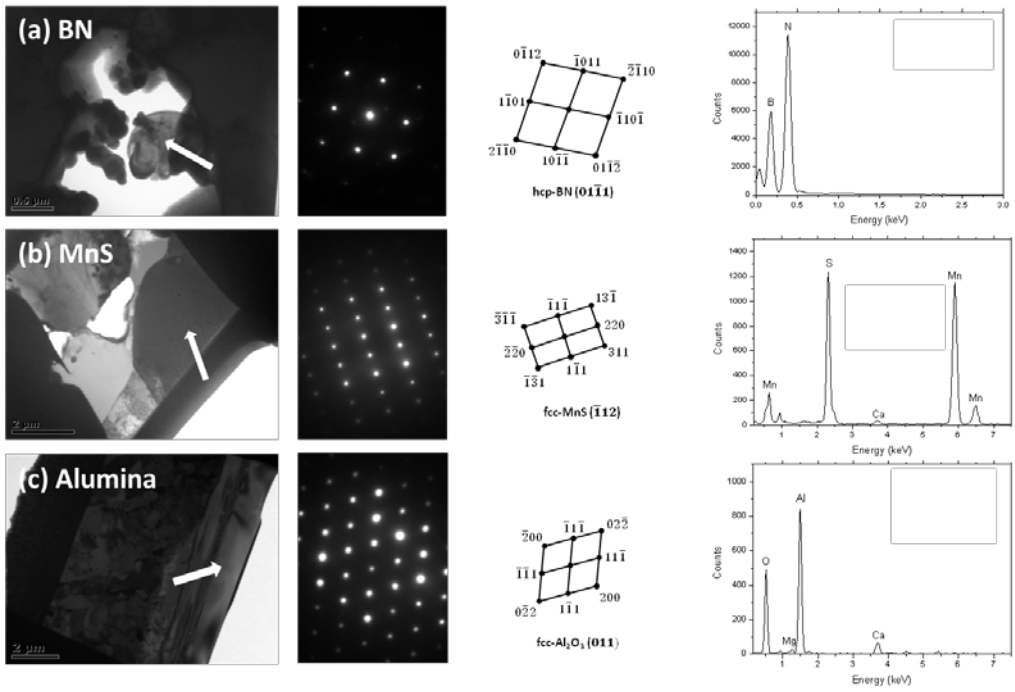

Figure 6: Bright field TEM images, SAD patterns and EDS spectra of BN (a), MnS (b) and alumina (c) type particles associated with cavities.

Boron Nitride Particles in Head Sections and Head-Gauge Transition Areas

Fig. 7 shows a low magnification in-lens SEM image taken in the head section of sample 650-A. No cavities were observed in the head section but BN particles are present and are highlighted by arrows in Fig. 7. Fig. 8 shows high magnification in-lens images of the BN particles and they can be seen to possess a characteristic surface texture and irregular shape that distinguishes them from other particle types.

The BN particles in the head-gauge transition area were also examined using in-lens SEM. In this area, which is expected to be exposed to a reduced creep stress compared with the gauge section, tiny cavities can be seen to be associated with the BN particles. This provides strong evidence that these particles provide the nucleation sites for creep cavities.

Fig. 10 shows the predicted weight fraction of phases present in the P92 steel composition A against temperature. In addition to the ferritic matrix, three secondary phases; Laves phase, $M_{23}C_6$ and VN-type MX, are predicted to form in the temperature range of the creep tests (550 to 650^{o}C). The lowest temperature boron nitride is predicted to form is 710^{o}C for composition A. No boron nitride precipitation is predicted within the temperature range of the creep tests (550 to 650^{o}C), which suggests that the boron nitride particles formed at higher temperatures during thermal processing. The B and N levels present in the steel compositions studied here are at a level where Sakuraya *et al*. [13] and Li *et al*. [14] predict BN could form depending on the thermal processing schedule used. Boron is added to improve the creep strength of P92 steels by suppressing the coarsening of $M_{23}C_6$ precipitates [12]. However, these benefits are not likely to be realised if the B is present primarily as coarse BN particles. Indeed these large hard irregularly shaped particles are likely to act as stress concentrators where cavities preferentially nucleate, as has been observed in this study.

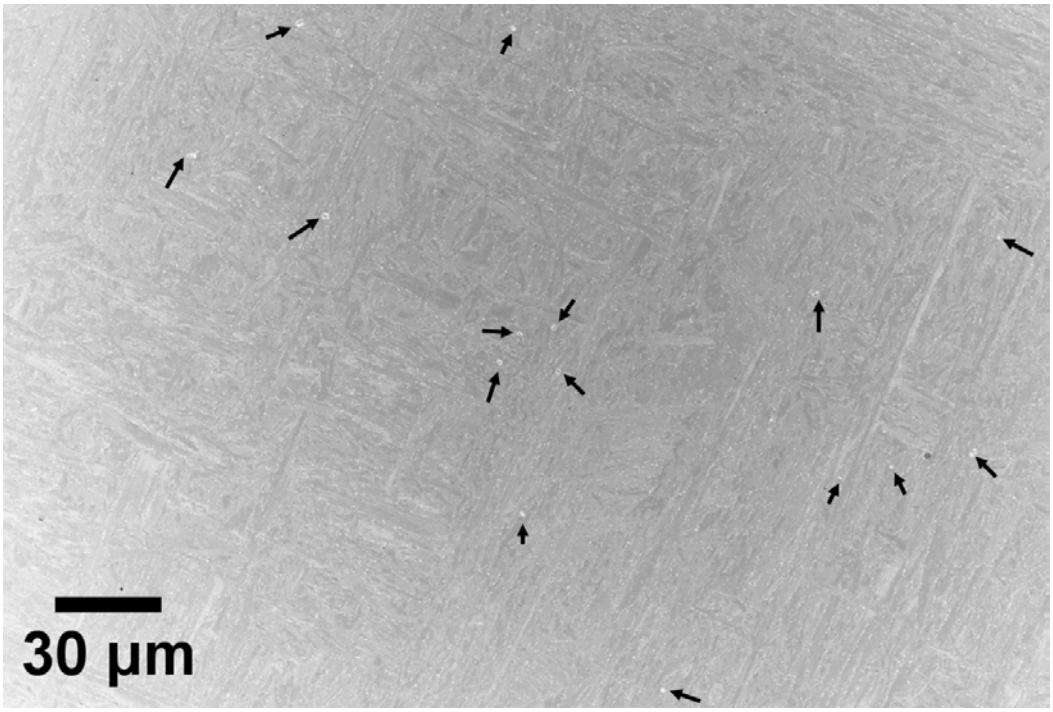

Figure 7: An in-lens SEM micrograph taken in the head section of sample 650-A, in which BN particles are indicated by arrows.

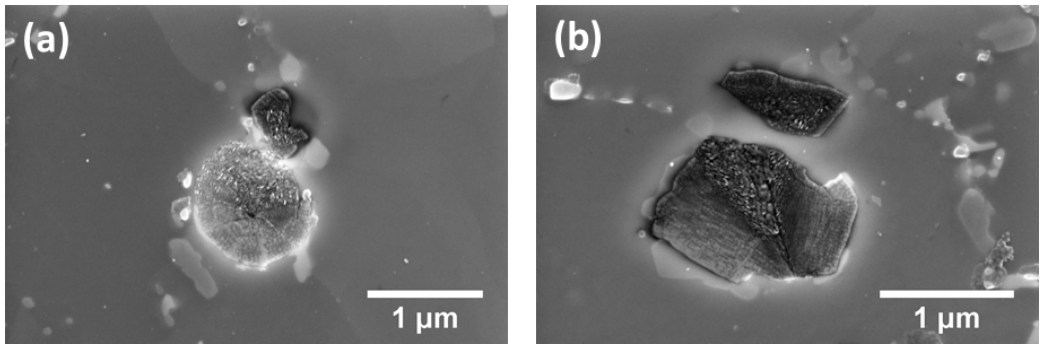

Figure 8: In-lens SEM micrographs of BN particles in the head section of sample 650-A.

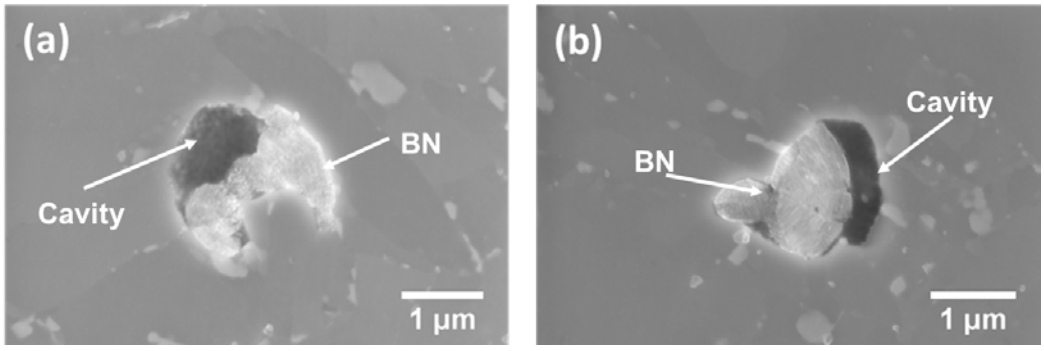

Figure 9: In-lens SEM micrographs of BN particles in the head-gauge transition area of sample 650-A.

CONCLUSIONS

Analysis of the creep cavities formed in P92 steel after exposure to a range of creep test conditions revealed that the majority of them were associated with hard ceramic particles. Chemical analysis of these hard ceramic particles revealed that the vast majority were BN in this case, although some Al_2O_3 and MnS particles were also observed. 3D analysis of the cavities and particles showed that they both had irregular shapes and that the particles often accounted for a significant fraction of the cavity volume. Additionally, very small cavities were found to be associated with the BN particles in the head-gauge transition area of the crept samples, indicating the onset of creep damage.

Analysis of the head sections using a combined in-lens SEM/EDS approach showed that BN particles were also present in the regions of the sample free from cavities. This provides evidence that the BN particles were introduced during the initial thermal processing of the steel rather than during creep exposure. This is supported by thermodynamic calculations which showed that BN is predicted to form at much higher temperatures than the samples were exposed to during the creep tests.

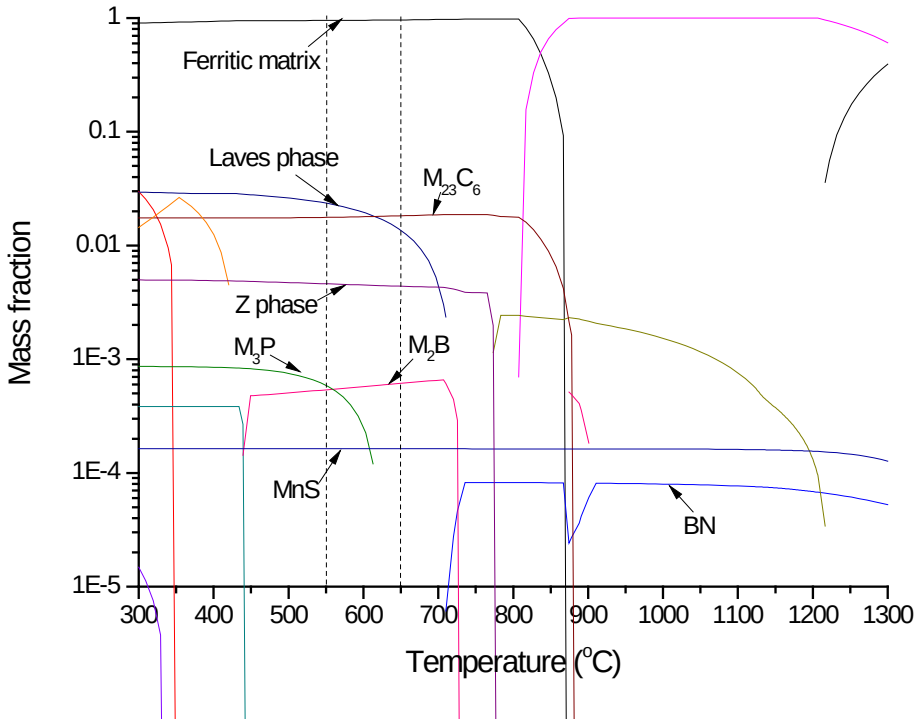

Figure 10: Thermodynamic simulation of composition A showing the mass fraction of the phases present as a function of temperature.

ACKNOWLEDGEMENTS

The authors would like to thank EPRI for the support of this project.

REFERENCES

[1] Masuyama F. ISIJ International 2001;41;612.
[2] Bhadeshia HKDH. ISIJ International 2001;41:626.
[3] Abe F. Materials Science and Engineering A 2001;319;770.
[4] Hong SG, Lee WB, Park CG. Journal of Nuclear Materials 2001;288;202.
[5] Cipolla L, Danielsen HK, Venditti D, Di Nunzio PE, Hald J, Somers MAJ. Acta Materialia 2010;58;669.
[6] Abe F. Metallurgical and Materials Transactions A 2003;34;913.
[7] Wu R, Sandström R. Materials Science and Technology 1995;11;579.
[8] Kassner ME, Hayes TA. International Journal of Plasticity 2003;19;1715.
[9] Lee JS, Armaki HG, Maruyama K, Muraki T, Asahi H. Materials Science and Engineering A 2006;428;270.
[10] Zhao Q, Li T, Deng X, Cheng D. Microstructural evolution of P92 steel during creep. In: Gandy D, Shingledecker J, Viswanathan R, editors. Proceedings of the 6th international

conference on advances in materials technology for fossil power plants, 31 August – 3 September 2010, Santa Fe, New Mexico, USA: ASM International; 2010. p. 693.
[11] Horiuchi T, Igarashi M, Abe F. ISIJ International 2002;42;67.
[12] Abe F. Procedia Engineering 2011;10;94.
[13] Sakuraya K, Okada H, Abe F. Energy Material 2006;1;158.
[14] Li L, MacLachlan R, Jepson MAE, Thomson RC. Metallurgical and Materials Transactions A 2013;44A;3411.
[15] Gregg JM, Bhadeshia HKDH. Acta Materialia 1997;45;739.
[16] Kaye & Laby, Tables of Physical & Chemical Constants, National Physical Laboratory. http://www.kayelaby.npl.co.uk/.